Hindawi
Shock and Vibration
Volume 2022, Article ID 9694576, 17 pages
https://doi.org/10.1155/2022/9694576

Research Article

Formation of an Explosively Formed Penetrator Warhead Using a Step-Shaped Charge

Weizhan Wang[1], **Zhigang Chen**[1], **Baoliang Yang**[2], **Tong Jing**[2], **Fangao Meng**[3] and **Taiyong Zhao**[1]

[1]*National Defense Key Discipline Laboratory of Underground Target Damage Technology, North University of China, Taiyuan, Shanxi 030051, China*
[2]*Xi'an Modern Control Technology Institute, Xi'an 710065, China*
[3]*Shandong North Binhai Machinery Co.ZiBo, Shandong 255000, China*

Correspondence should be addressed to Weizhan Wang; 530056679@qq.com

Received 20 November 2021; Revised 30 March 2022; Accepted 12 May 2022; Published 21 June 2022

Academic Editor: Chang-Ping Yi

Copyright © 2022 Weizhan Wang et al. This is an open access article distributed under the Creative Commons Attribution License, which permits unrestricted use, distribution, and reproduction in any medium, provided the original work is properly cited.

In this study, the formation mechanism of an explosively formed penetrator (EFP) with tail fins was analyzed. Through static denotation and dynamic flight tests, the feasibility of using a step-shaped liner during the formation of an EFP with tail fins was verified. The influences of the step depth, h, and the step angle, Φ, on the flight stability were then explored. Based on the consistency between the numerical simulation and experimental results, the influences of the step-shaped liner's spherical arc radius, number of steps, and wall thickness on the formation and flight stability of an EFP with tail fins were further studied. The results showed that a T2 copper step-shaped liner performed better than a H90 brass liner. Compared with a hemispherical liner with an equal wall thickness, the step-shaped liners resulted in EFPs with initial angular velocities and relatively better flight stability. Moreover, a greater initial angular velocity led to a higher EFP landing accuracy.

1. Introduction

The explosively formed penetrator (EFP) with tail fins is a widely used warhead in terminal-sensitive ammunition and dexterous ammunition because of its long-distance stable flight capabilities and its ability to destroy targets. Using a well-designed aerodynamic profile is a key approach to improve the stability of EFP flights and ensure their penetration power. Researchers have conducted extensive experiments and theoretical research on this topic, mainly focused on the detonation mode control, and drug cover structure and charge structure design three aspects.

In the early stages of EFP research, William [1] used a combination of numerical simulations and experimental methods to obtain a pleated-tail EFP with good aerodynamic shapes by designing anisotropic charges and liner structures. Berner and Flec [2] found that the drag on the EFP decreases as the number of tails increases, while the flight drag on the EFP increases with the increase in the tail height. Donneaud [3] found that an EFP with an oblique tail has lower velocity loss and higher flight stability during flight than traditional EFP. The EFP can be rotated in the air to improve its aerodynamic characteristics and accuracy on the target.

With the in-depth study of EFPs, many recently published studies were based on forming theory. Effects of the liner material, structure, and explosive detonation methods have also been studied, which have important effects on the tail EFP [4]. Wu et al. [5] investigated the EFP penetration performances in armor plates by fitting the velocity decay equation using a combination of similarity theory and numerical simulations and verified the engineering applicability of the velocity decay equation. Hussain et al. [6, 7] investigated the relationships between the velocity, pressure, density, internal energy, temperature, and aspect ratio of

EFPs and found that Fe and Ta pill-type shield materials produced the largest magnitude and fluctuations of the impact pressure, while copper yielded the smallest axial pressure variations and the largest axial aspect ratio. Li et al. [8, 9] studied the influence of the structural parameters of the drug-type shield on the flight stability of EFPs by ballistic flight experiments and learned that the flight stability can be effectively improved when the liner wall thickness is 0.046 times the charge diameter. Cardoso and Teixeira-Dias [10, 11] examined the applicability of LS-DYNA software for solving Lagrange's formula in the formation, flight, and penetration of explosively formed projectiles, which can reproduce the explosively formed projectile formation conditions and ballistic flight capabilities. This numerical simulation method can evaluate different structures, materials, and blast conditions of the charge hood.

Li et al. [12] investigated the feasibility of polygonal charge shell layers to form EFP with large aspect ratio and found that hexagonal polygonal charges can form EFP structures with better aerodynamic performance. Baburin et al. [13] developed a model for forming a tilted-fold tail EFP, studied the influence of the tail on the change in the aerodynamic coefficients for a wide range of head-on angles, and calculated the angular velocity of the axial rotation of the tilted-fold tail EFP based on Newton's method. Ding et al. [14] used stress-wave theory to analyze the long-rod fracture mechanism of explosively formed projectiles in the forming stage and experimentally verified the critical velocities of copper and tantalum foil forming. Jie et al. [15] investigated the formation mechanism of a double-curvature charge-hood explosively formed projectile under the effect of a positive oblique reflection overpressure. Liu et al. [16] designed a double-layer polymeric charge (DLPC) with an outer layer of high explosive velocity and an inner layer of low explosive velocity and compared the forming processes and penetration performances of an explosively formed projectile for a DLPC and ordinary polymeric charge (OPC). Yang and Lin [17] analyzed the forming process of EFPs with axisymmetric variable-thickness liners and found that the steady-state velocity of the EFP was the largest when the edge thickness of the liner was used and the steady-state velocity was the smallest when the equal-thickness liner was used.

Researchers have extensively studied the EFP forming process and have achieved a certain understanding of the mechanism and characteristics of EFP forming. However, previous experiments and theoretical studies did not report the forming characteristics of EFPs with free-spinning tail fins. Based on previous research [18, 19], static explosion forming and dynamic flight tests on the liner structure of a stepped liner were investigated in this study. We obtained an EFP with tail fins with a certain initial rotational angular velocity and compared and analyzed the light stability of the EFP formed by the stepped liner and a conventional liner. Analysis was performed to investigate the influences of the structural parameters of the stepped liner on the forming and flight stability characteristics of the EFP. These results provide a reference for the design of dexterous ammunition warheads.

2. Explosively Formed Penetrator (EFP) Molding Theory Analysis

Using Prandtl–Meyer piston theory [20] to describe the space effect of a driven object of the detonation product, a two-dimensional approximation model can be obtained. To accurately describe the motion of the driven object, the detonation product must be accurately described. The state of motion is used to determine the explosion pressures acting on the driven object. The final pressure P (MPa) acting on the object is as follows:

$$P = p\frac{p_j}{p_j} = \frac{p}{p_1}\frac{p_1}{p_j}p_j = \left[\frac{0.5(\gamma+1)Ma_1^2}{1+0.5(\gamma-1)Ma_2^2}\right]^{\gamma/\gamma-1} p_j. \quad (1)$$

The area sum of the projections of all the spherical surfaces along the liner axis was a fixed value, which can be expressed as follows:

$$a(S_s \cos\theta_1 + S_l \cos\theta_2) = \pi R^2, \quad (2)$$

where a is the number of steps, S_s is the area of the small spherical surface (m^2), S_l is the area of the large spherical surface (m^2), $\theta_1 = \arctan f(x) - g(x)/\varphi x$ (°), and $\theta_2 = \arctan f(x) - g(x)/(\pi/3 - \varphi)\, x$ (°). Φ represents the step offset angle (°), $f(x) = \sqrt{SR_1^2 - x^2}$ is the projection equation for the arc with a radius of SR_1 in the front view, and $g(x) = \sqrt{SR_2^2 - x^2}$ is the projection equation for the spherical arc with a radius of SR_2 in the front view. SR_1 and SR_2 are the spherical arc radii on both sides of the ladder (m).

The area of the small spherical surface was calculated as follows:

$$S_s = \int_r^R \frac{f(x) - g(x)}{\cos\alpha \sin\theta_1}\mathrm{dx}, \quad (3)$$

where R is the radius of the pharmacophore (m), r is the radius of the spherical arc at the top of the pharmacophore (m), and h is the depth of the pharmacophore steps (m). Then, the tangential torque of the small spherical surface can be calculated as follows:

$$\overrightarrow{M_s} = \overrightarrow{F_s} \times \overrightarrow{r} = \left(\overrightarrow{P} * S_s\right) \times \overrightarrow{r} = \begin{vmatrix} \overrightarrow{i} & \overrightarrow{j} & \overrightarrow{k} \\ \left[\frac{1}{2}(r+R)\right] & 0 & 0 \\ PS_s\cos\gamma_1 & 0 & PS_s\sin\gamma_1 \end{vmatrix}, \quad (4)$$

where P represents the pressure on the liner (MPa), and $\gamma_1 = 90 - \theta_1/2$, where γ_1 is the angle between P and the horizontal direction (°).

The liner finite element area for the large spherical surface is expressed as follows:

$$S_l = \frac{\pi R^2}{a\cos\theta_2} - \frac{S_s\cos\theta_1}{\cos\theta_2} = \frac{\pi R^2 - aS_s\cos\theta_1}{a\cos\theta_2}. \quad (5)$$

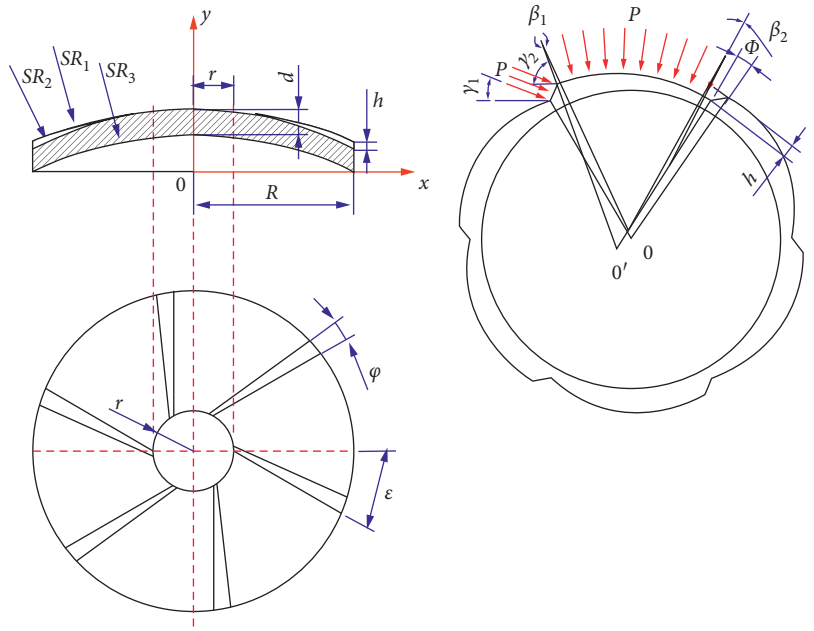

FIGURE 1: Schematic diagram of the structure of a single-sided step-shaped liner. (a) Front view. (b) Top view.

Then, the tangential torque for the large spherical surface can be obtained as follows:

$$\overrightarrow{M_l} = \overrightarrow{F_l} \times \overrightarrow{r} = \left(\overrightarrow{P} * S_l\right) \times \overrightarrow{r} = \begin{vmatrix} \overrightarrow{i} & \overrightarrow{j} & \overrightarrow{k} \\ \frac{1}{2}\left(SR_1 \sin \beta_1 + SR_2 \sin \beta_2\right) & 0 & 0 \\ PS_l \cos \gamma_2 & 0 & PS_l \sin \gamma_2 \end{vmatrix}, \tag{6}$$

where $\gamma_2 = 90 + \theta_2/2$, where γ_2 is the angle between the pressure of the large spherical surface P and the horizontal direction (°), and β_1 and β_2 are the circle center offset angles of the large and small spherical surfaces (Figure 1(b); °), respectively. The angular acceleration is expressed as follows:

$$\begin{aligned} \alpha_r = \frac{\left|\overrightarrow{M_r}\right|}{I} = \frac{\left|\overrightarrow{M_l} - \overrightarrow{M_s}\right|}{ml^2} &= \frac{\left\| \begin{matrix} \overrightarrow{i} & \overrightarrow{j} & \overrightarrow{k} \\ 1/2\left(SR_1 \sin \beta_1 + SR_2 \sin \beta_2\right) & 0 & 0 \\ PS_l \cos \gamma_2 & 0 & PS_l \sin \gamma_2 \end{matrix} \right| - \left| \begin{matrix} \overrightarrow{i} & \overrightarrow{j} & \overrightarrow{k} \\ [1/2(r+R)] & 0 & 0 \\ PS_s \cos \gamma_1 & 0 & PS_s \sin \gamma_1 \end{matrix} \right\|}{ml^2} \\ &= \frac{\left\{1/2\left(SR_1 \sin \beta_1 + SR_2 \sin \beta_2\right) + [1/2(r+R)]\right\} * PS_l \sin \gamma_2 + PS_s \sin \gamma_1}{ml^2}, \end{aligned} \tag{7}$$

where l is the distance from the liner equivalent center of mass to the axis (m) and m is the mass of the liner (kg). Then, the EFP initial axial angular velocity can be calculated as follows:

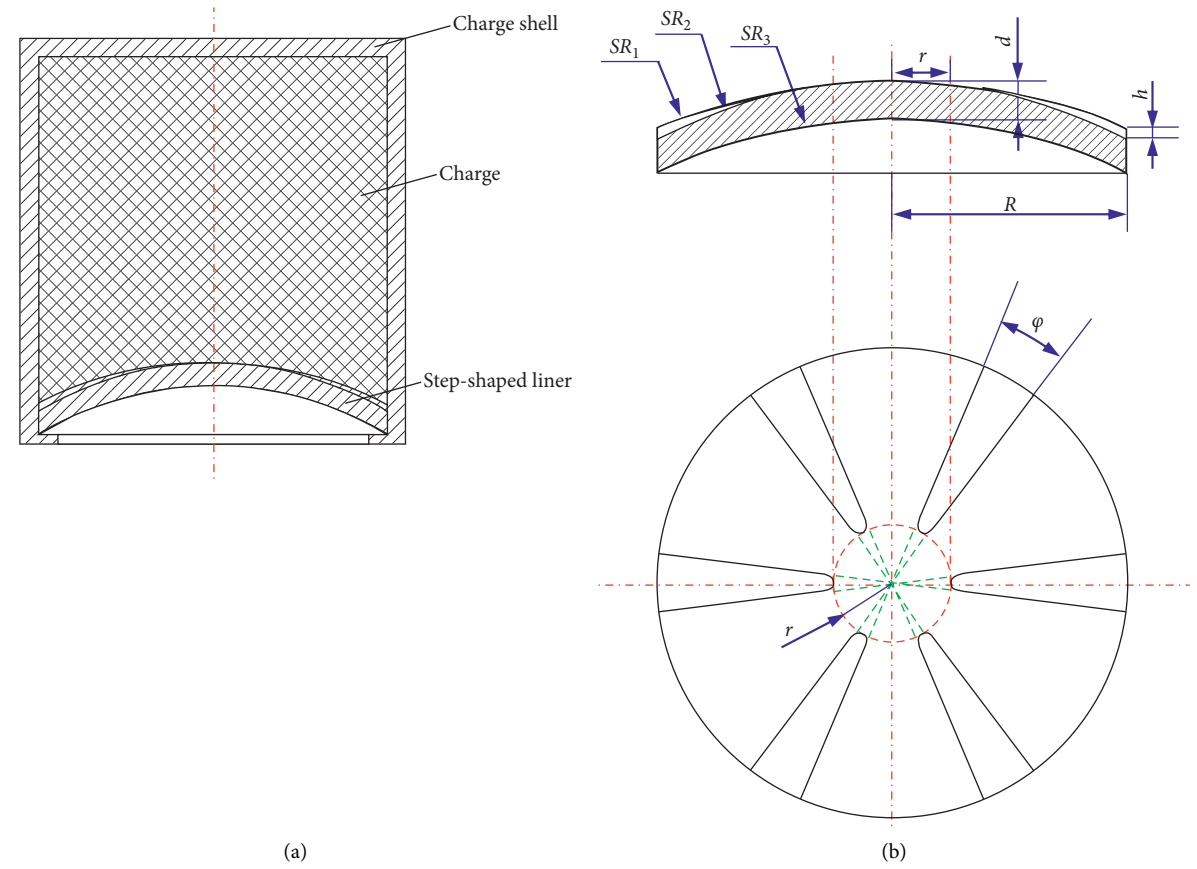

Figure 2: Schematic diagram of the shaped charge (a) and schematic diagram of the step-shaped liner (b).

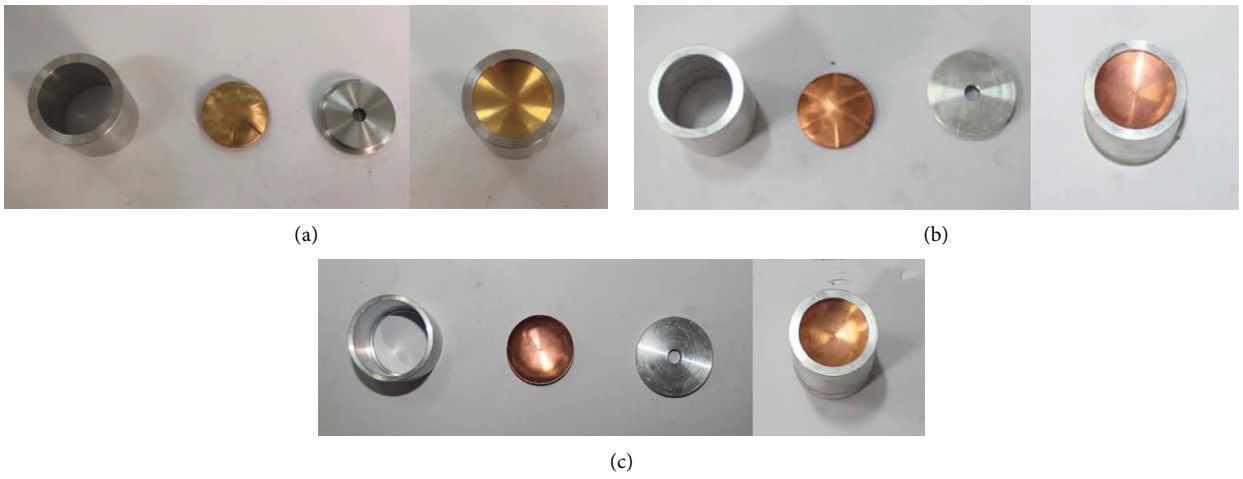

Figure 3: Photograph of the shaped charge: (a) H90 brass step-shaped charge, (b) T2 copper step-shaped charge, and (c) T2 copper-shaped charge with the constant wall thickness.

$$\omega = \int_0^{t_0} \alpha_r \mathrm{d}t, \tag{8}$$

where t_0 represents the liner collapse time (explosive blast wave on the liner loading time t_0 created by the charge size and explosive burst speed s). The axial force is given as follows:

$$F_a = PS_c + aPS_o = P\pi r^2 + aPS_l \sin\gamma_2 \cos\theta_2 + aPS_s \sin\gamma_1 \cos\theta_1. \tag{9}$$

Then, the EFP axial velocity can be calculated as follows:

$$v_a = \int_0^{t_0} \frac{F_a}{m} \mathrm{d}t. \tag{10}$$

Table 1: Structural parameters (T2 copper liners and H90 brass liners).

Parameters	R (mm)	d (mm)	SR_1 (mm)	SR_2 (mm)	SR_3 (mm)	r (mm)	h (mm)	Φ	m (g)
T2	20	2.66	42.66	52.6	40.88	5	0.97	6°	29.8
H90	20	2.66	42.66	52.6	40.88	5	0.97	6°	29.8

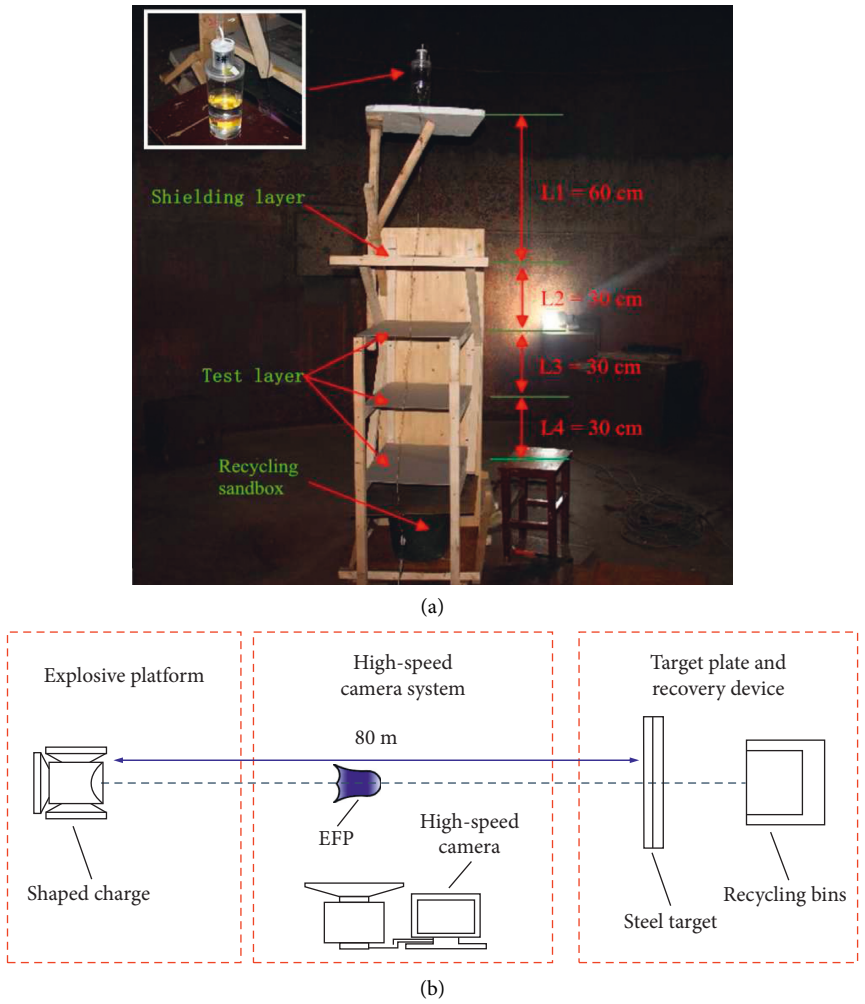

Figure 4: (a) Layout of the explosively formed penetrator (EFP) formation test site. (b) Schematic diagram of the EFP shooting accuracy test system.

Based on equations (1)–(10), the relationships of the EFP initial angular velocity and the axial flight velocity with the step depth h, step offset angle Φ, step rotation angle ε, liner mass m, number of steps a, and radius of the spherical surface r were determined:

$$v_a = \int_0^{t0} \frac{P\pi r^2 \cos\theta_2 + P\left[\pi R^2 - a\left(\int_r^R h/\cos\varepsilon \sin\theta_1 \mathrm{d}x\right)\cos\theta_1\right]\sin\gamma_2 + aP\left(\int_r^R h/\cos\varepsilon \sin\theta_1 \mathrm{d}x\right)\sin\gamma_1\cos\theta_2}{m\cos\theta_2}\mathrm{d}t, \tag{11}$$

$$\omega = \int_0^{t_0} \frac{\{1/2\,(SR_1\sin\beta_1 + SR_2\sin\beta_2) + [1/2\,(r+R)]\} * P\left[\pi R^2 - a\left(\int_r^R h/\cos\varepsilon \sin\theta_1 \mathrm{d}x\right)\cos\theta_1\right]\sin\gamma_2 + aPS_s\sin\gamma_1\cos\theta_2}{a\cos\theta_2 ml^2}\mathrm{d}t. \tag{12}$$

(11) indicates that there is a positive correlation between the axial speed v_a, the step depth h, and the step rotation angle, ε. However, (12) indicates that the EFP axial angular velocity is positively correlated with the number of steps a and the step

Table 2: Test conditions.

No.	B-1#	B-2#	B-3#	B-4#	B-5#	B-6#
Parameter	$m = 29.7$ g $h/d = 0.364$ $\Phi = 12^\circ$	$m = 29.8$ g $h/d = 0.364$ $\Phi = 6^\circ$	$m = 29.5$ g $h/d = 0.2$ $\Phi = 12^\circ$	$m = 30.3$ g $h/d = 0$ $\Phi = 0^\circ$	$m = 29.7$ g $h/d = 0.2$ $\Phi = 6^\circ$	$m = 30.3$ g $h/d = 0$ $\Phi = 0^\circ$

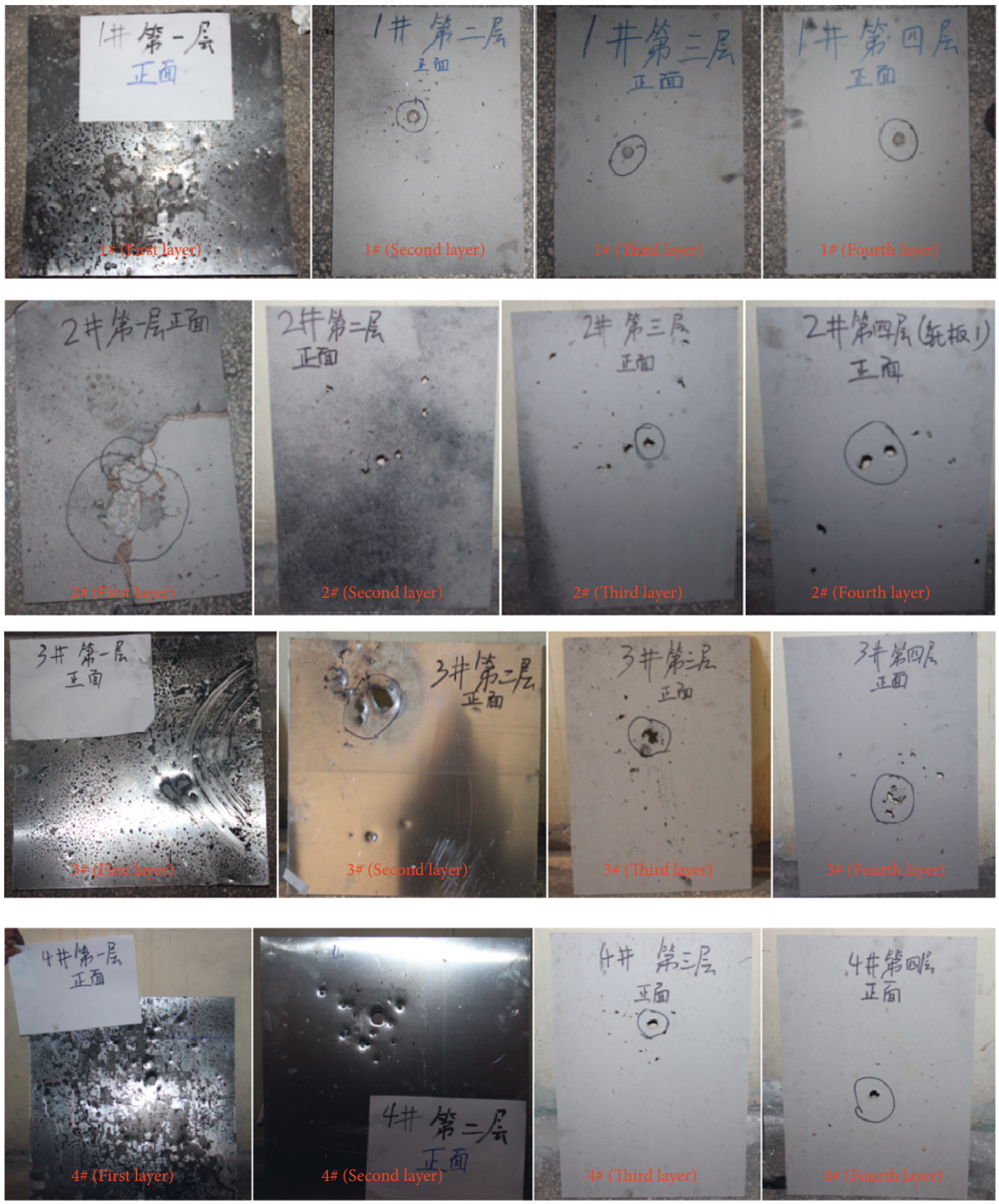

Figure 5: Overview of the retrieved target plates.

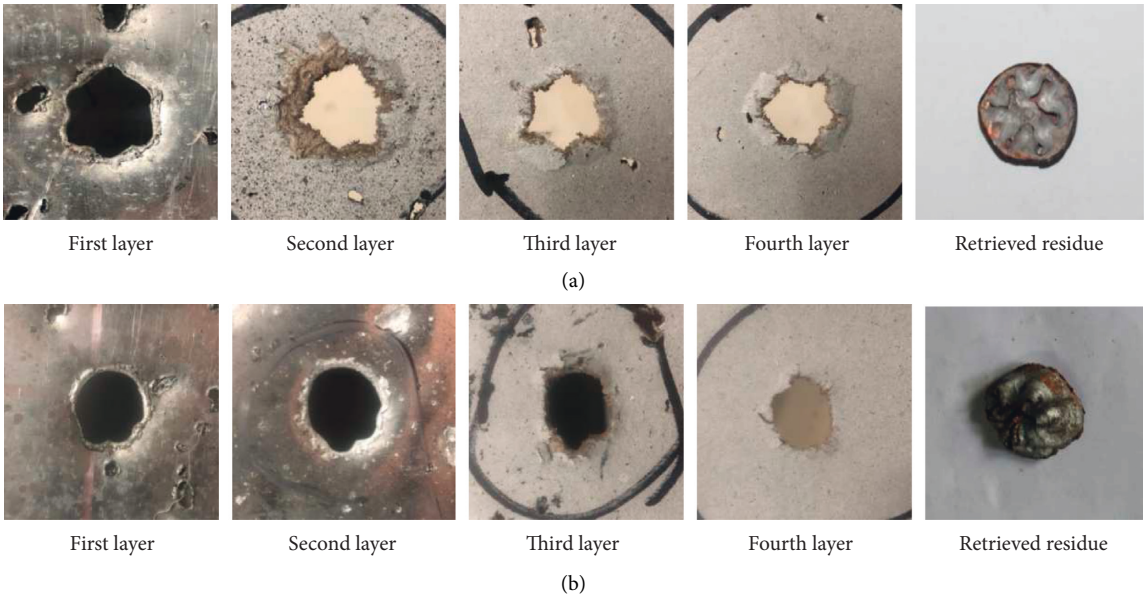

Figure 6: EFPs and perforation morphology residues for tests (a) A-1# and (b) A-4#.

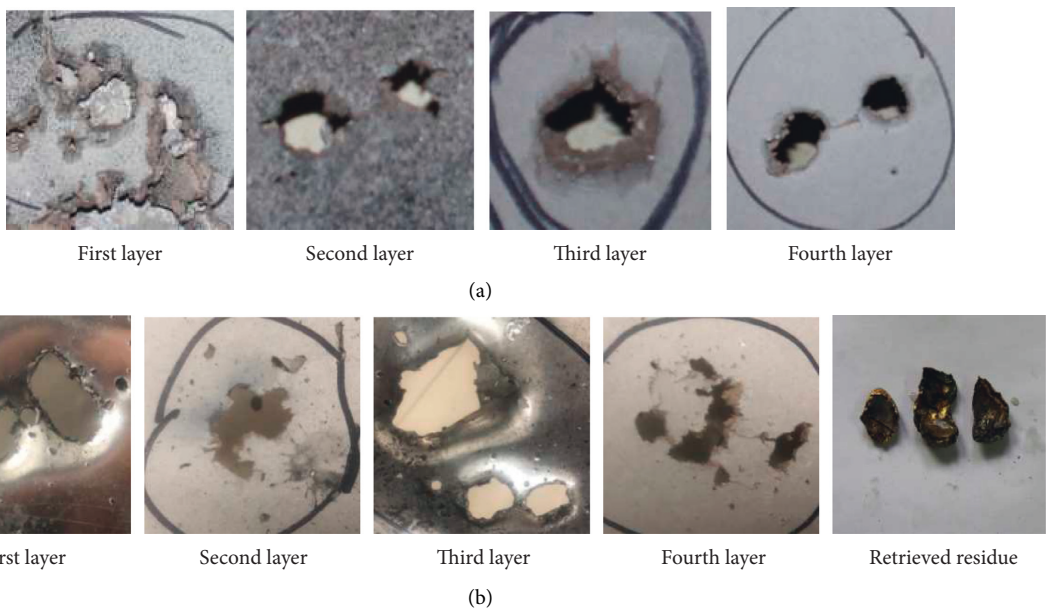

Figure 7: Perforation morphologies of the target plates from tests. (a) A-2# and (b) A-3#.

rotation angle ε and negatively correlated with the step offset angle Φ and the mass of the liner m. We found the solutions of these equations using the numerical calculation software MATLAB. In addition, we carried out the structural design of the stepped liner based on the above conclusions.

3. EFP Formation and Impact Test

3.1. Shaped Charge. Figure 2 presents a schematic diagram of the structure of the shaped charge and an image of the actual model. The structural dimensions include the radius of the liner (charge radius) R, the wall thickness d, the radii of the step-shaped liner's outer surfaces SR_1 and SR_2, the radius of the inner surface SR_3, the step depth h, the radius of the spherical arc r, the step angle Φ, and the step rotation angle ε (0°). The charge height was twice the charge radius. Figure 3 shows three types of step-shaped liners: one was made of H90 brass (Figure 3(a)) and the others were made of T2 copper (Figures 3(b) and 3(c)). The wall of the shaped charge shell was composed of 2A12 aluminum and had a wall thickness of 3.5 mm.

3.2. Experimental Setup

3.2.1. EFP Forming Test Overview. The EFP denotation tests were conducted at the Key National Defense Laboratory for

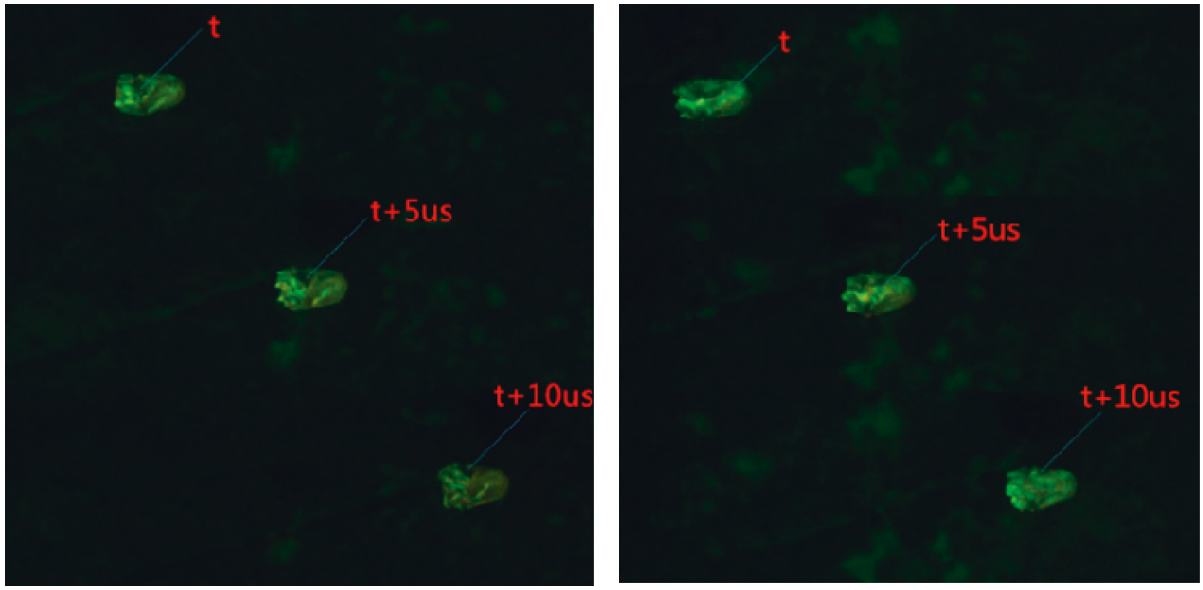

Test B-1# EFP (a)

Test B-3# EFP (b)

Figure 8: EFP flight patterns for tests. (a) B-1# and (b) B-3#.

Underground Target Damage Technology at the North University of China. A total of four denotation tests were performed using the step-shaped charge. Tests A-1# and A-4# used T2 copper liners, and tests A-2# and A-3# used H90 brass liners. An EFP perforation shape was obtained using a 2-mm 2A12 aluminum alloy target plate and a 3-mm cardboard target plate. The target spacing was $L_2 = L_3 = L_4 = 30$ cm, and the height was $L_1 = 60$ cm. A recovery sandbox was placed below the targets. The structural parameters used for the test liner (brass and purple copper liner) are shown in Table 1. The layout of the test site is shown in Figure 4(a).

3.2.2. EFP Flight Test Overview. A total of six EFP shots were fired to test the aiming accuracy, including four shots with step-shaped liners and two shots with constant-thickness liners. The parameters of the shaped charge were $R = 20$ mm, $d = 2.66$ mm, $SR_1 = 42.66$ mm, $SR_2 = 52.6$ mm, $SR_3 = 40.88$ mm, $r = 5$ mm, and $m = 29.8 \pm 0.5$ g. The values of the h/d ratio and Φ are shown in Table 2.

The denotation point was 80 m from the target, which was 50 mm thick and composed of 616 armor steel. A high-speed camera was used to capture the EFP flight behavior. The layout of the test site is shown in Figure 4(b).

3.3. Results and Discussion

3.3.1. EFP Formation Tests. Figure 5 shows the results of the four EFP formation tests with shaped charges. The shapes of the EFPs for tests A-1# and A-4# on the four target plates were circular perforations with multiple small perforations. However, the EFPs for tests A-2# and A-3# on the four target plates had multiple large and small perforations, with no evident regularity in the perforation shape.

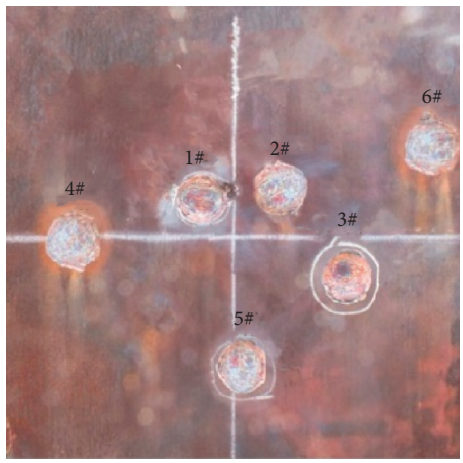

Figure 9: EFP landing points for tests B-1#–B-6#.

Figure 6 shows the perforation results for tests A-1# and A-4# using T2 step-shaped liners. In particular, the EFP formed by the T2 copper step-shaped liner in test A-1# had a six-petal perforation with a certain spiral angle on the first aluminum target (Figures 6(a) and 6(b)). On the second, third, and fourth cardboard targets, the perforation shapes were always spiral six-petal shapes, consistent with that on the aluminum target. The EFP residues retrieved from tests A-1# and A-4# showed that, although there was plastic deformation, the tail fins for one EFP had folds (test A-4#), and the tail fins for the other EFP had a spiral angle (test A-1#). Thus, it was concluded that tail-shaped EFPs with spiral angles were formed by the T2 copper step-shaped liner.

Table 3: Test results.

No.	B-1#	B-2#	B-3#	B-4#	B-5#	B-6#
Type of liner	Step	Step	Step	Constant wall thickness	Step	Constant wall thickness
Velocity (m/s)	1423	1401	1439	1422	1411	1428
Angular velocity (rad/s)	328	221	179	0	135	0
Deviation displacement, L (cm)	3.4	4.5	8.1	11.2	8.8	15.6

Figure 7 presents the perforation results for tests A-2# and A-3# using H90 step-shaped liners. Figure 7(a) shows that the first aluminum target had two large elliptical perforations, while the perforations on the second, third, and fourth layers of the target plate were irregular. The perforations shown in Figure 7(b) were also irregular. Based on the EFP residue retrieved from the test results shown in Figure 7, it was concluded that the H90 brass material did not form tail-type EFPs. This was because H90 brass is more brittle than T2 copper. Stress concentrated at the H90 brass liner step under the detonation wave loading effect, causing fracture. Although H90 brass could be used as the liner material for some shaped charges, based on these results, it is not suitable for step-shaped liners.

3.3.2. EFP Trajectories and Impacts. Figures 8(a) and 8(b) show the EFP flight behaviors at different times during tests B-1# and B-3#. The EFP flight trajectories were straight, and the tail fins were shaped like uneven folds. Marking an EFP tail fin showed its rotation at different times ($\Delta t = 5\,\mu$s). The results suggested that during the EFP formation process, an initial angular velocity was produced from the slippage effect of the denotation wave [17].

Figure 9 shows the distribution of the EFP landing points 80 m from the denotation point. Table 3 shows the test results. Figure 10 presents a schematic diagram for the measurement of the EFP rotational angular velocity. By marking the EFP tail fin in the image, the tail fin liner displacement was measured at adjacent times. The rotation angle of the tail fin was obtained based on the known tail fin radius, and it was subsequently used to calculate the angular velocity.

Table 2 shows that the EFP in test B-1# had the best landing accuracy and the largest angular velocity, followed by the EFPs in tests B-2#, B-3#, and B-5#. The lowest accuracy was observed for the EFPs in tests B-4# and B-6#. Moreover, the deviations from the target points for the EFPs formed using the equal-thickness liners were larger than those for the EFPs formed using the step-shaped liners. Tests B-1#, B-2#, B-3#, and B-5# used step-shaped charges with different step depths h and step angles Φ, and their landing accuracies were different from each other.

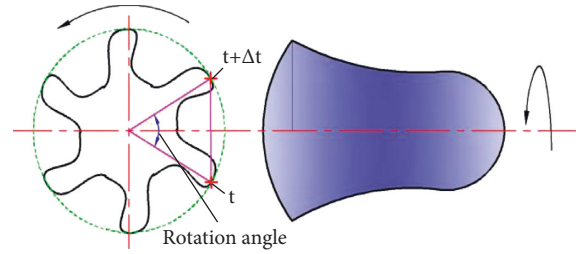

Figure 10: Schematic diagram for the measurement of the EFP angular velocity.

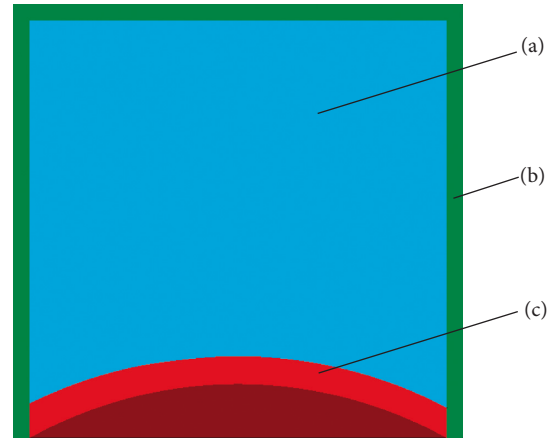

Figure 11: Finite element model.

4. Numerical Simulations and Comparisons

4.1. Overview of the Numerical Simulations

4.1.1. Modeling. To accurately describe the EFP formation process, a 1 : 1 three-dimensional finite element model was developed. The model was meshed using SOLID164 eight-node hexahedral elements [20, 21]. The grid cell size range was 0.1–0.2 mm. The Lagrangian algorithm was used for the explosive, charge liner, and shell, and surface-to-surface contact was used. The denotation began from the center of the charge. The LS-DYNA software was used to simulate the formation of a tail-type EFP and the perforations on the target plates [22]. The finite element model for the step-shaped charge is shown in Figures 11 and 12.

4.1.2. Material Parameters. The liner material was T2 copper, the charge's shell was 2A12 aluminum, and the materials were described using the Johnson–Cook model and the Grüneisen equation of state. The primary charge was an 8701 explosive, which was described by the high explosive burn material model and the Jones–Wilkins–Lee equation of state. The material parameters were taken from a previous report [18].

4.2. Formation and Flight Process

4.2.1. Formation Process. Figure 13 shows the EFP formation process when a step-shaped liner was used. The step structure was located on the outer surface at the boundary

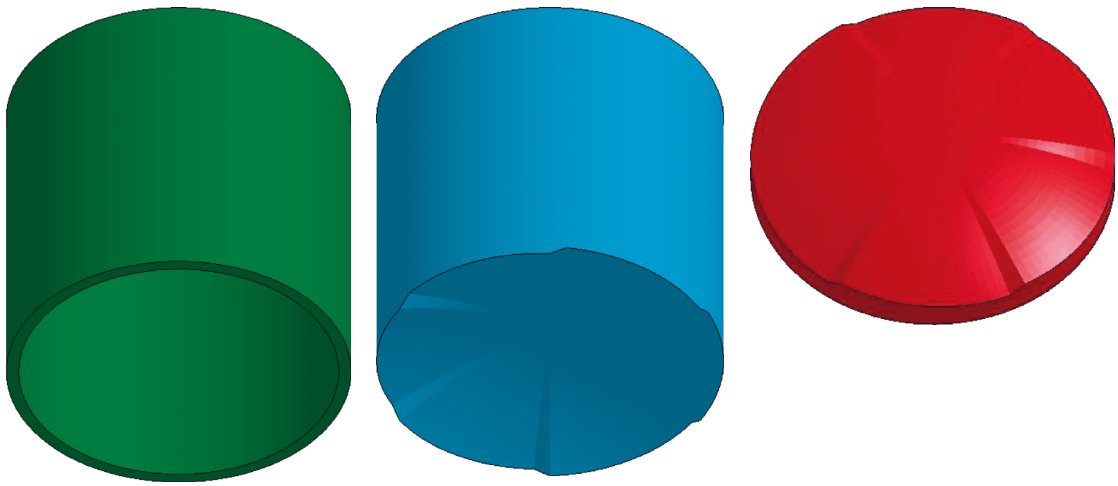

Figure 12: Finite element model of an EFP-shaped charge: (a) shell, (b) charge, and (c) liner.

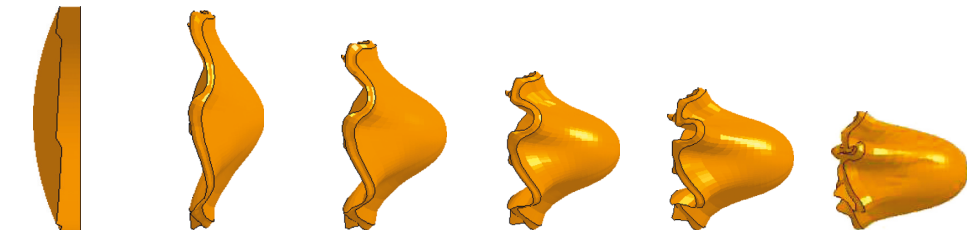

Figure 13: EFP formation process for a step-shaped liner.

between the spherical surfaces with different radii. The upper side of the liner had a large wall thickness, and the elements shrank radially during the formation process, resulting in a concave-groove tail fin structure. The wall thickness at the lower side of the liner was relatively small. During the EFP formation process, the elements expanded and folded radially to form a convex tail fin structure ($t = 0$–$100\,\mu s$). Because of the resistance characteristics of the liner material [23–25], the radial contracting and expanding elements shifted to a certain extent and then stopped moving. At this point, an EFP with a folded spiral tail fin was formed ($t = 120\,\mu s$). Meanwhile, during the EFP molding process, the EFP head velocity first increased ($t = 0$–$60\,\mu s$) and then gradually decreased ($t = 60$–$100\,\mu s$), and finally, the overall EFP velocity stabilized ($t = 120\,\mu s$).

Figure 14 shows the results of the numerical simulations and experiments (A-1#). These perforations had morphologies that were essentially the same as the perforation morphologies on the first four target plates, with no significant differences. The EFP tail fin did not deform after passing through the first 2-mm aluminum target, indicating that the formed EFP tail fin had a good structural strength. The perforations on the four target plates all had six-petal shapes with distinct spiral characteristics. The perforation patterns and sizes in the experimental results were in good agreement with the numerical simulation results.

Figure 15 shows the dynamic EFP pattern captured by the high-speed camera and the EFP residue retrieved after the static denotation. The EFP shapes for tests A-1# and A-4# indicated that the step-shaped liners formed EFPs with spiral tail fin structures, and the number of tail fins was equal to the number of steps. Spiral tail fin grooves with certain depths and spacing formed between adjacent fins. The folded tail fin grooves were closed in the radial direction and ran along the EFP axis. The spiral tail fins were in a convex shape in the radial direction. The EFP morphology in the experimental results is similar to the numerical simulation results, and the EFP flight velocities (1401 m/s and 1411 m/s) obtained from the tests in the experimental results are basically consistent with the numerical simulation results (1473 m/s and 1433 m/s), and the flight speed of the molded EFP in the test was in good agreement with the numerical simulations.

4.2.2. Flight and Impact Processes. The results in Section 2 showed that, for the same step depth, the EFP initial angular velocity increased with an increase in the step angle. For the same step angle, the EFP initial angular velocity increased with an increase in the step depth.

Figure 16 shows the comparison between the numerical simulations and the experimental results and the theoretical calculations. The variations of the EFP angular velocity

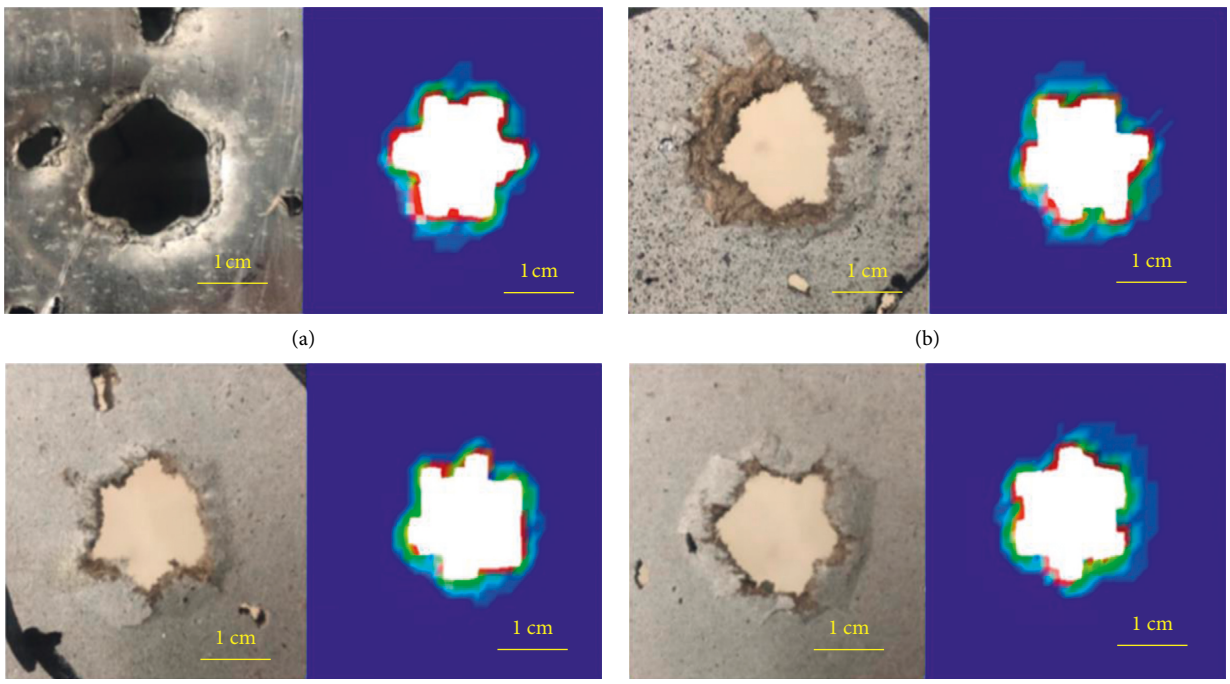

Figure 14: Comparison between experimental and simulation results: (a) first layer, (b) second layer, (c) third layer, and (d) fourth layer.

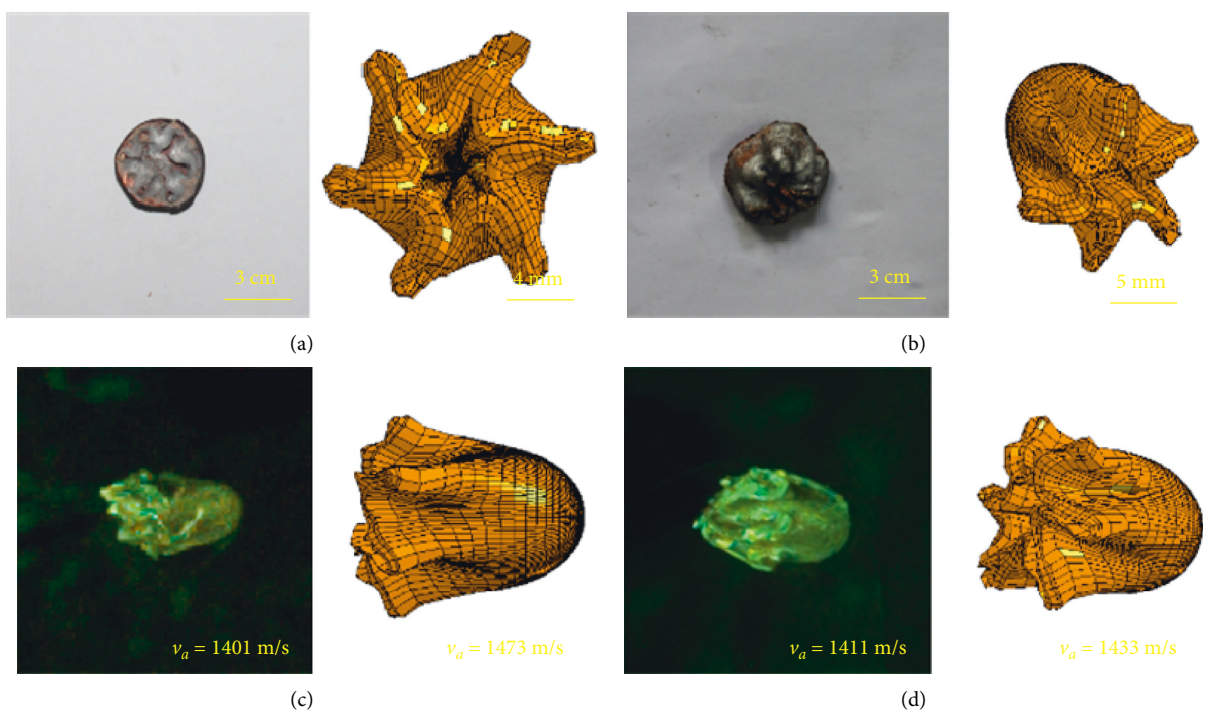

Figure 15: Comparison between the experiments and the simulation: EFP formation tests. (a) A-1# and (b) A-4#; EFP trajectories and impacts (c) B-2# and (d) B-5#.

during the numerical simulation were consistent with those in the experiments and theoretical calculation results, which verified the results from a previous study [20]. Therefore, the simulation method and theoretical calculation model used in this study are reliable.

Figure 17 shows the relationship between the deviation of the EFP from its target point and the angular velocity. When the step angle and step depth changed, the EFP axial velocity was not significantly affected. When the angular velocity of the EFP increased, the distance between the

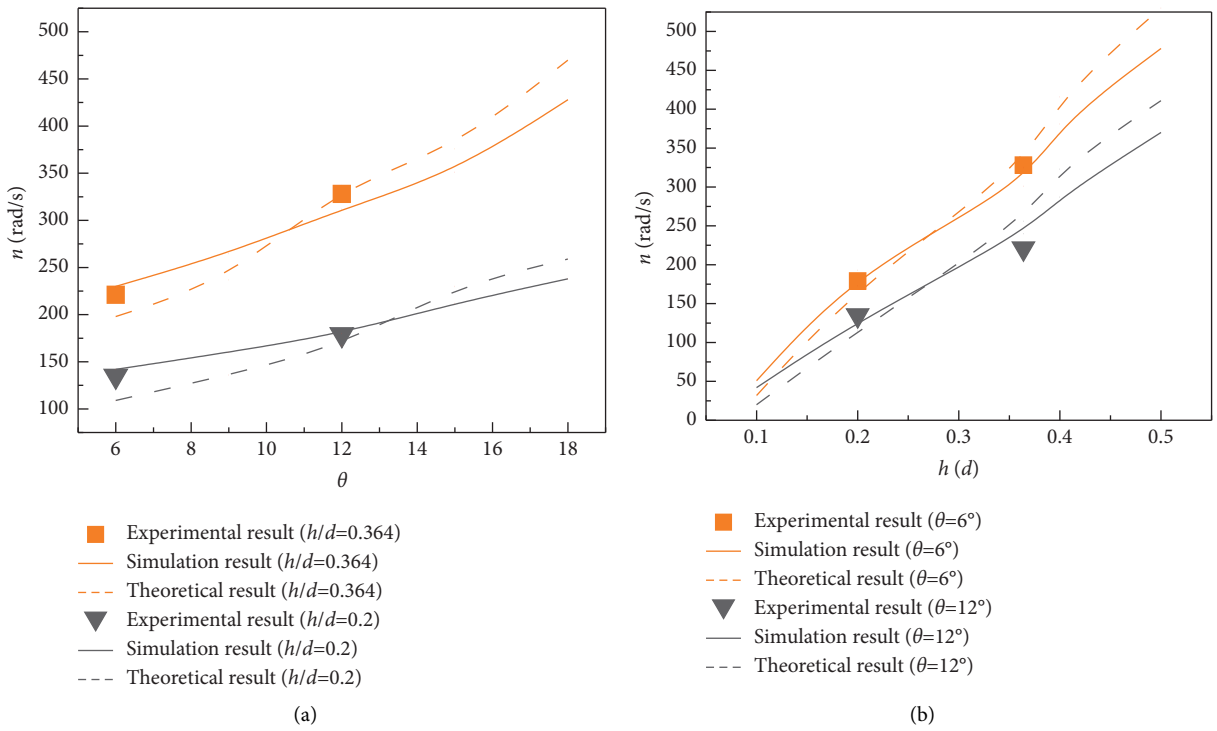

Figure 16: Comparison between experimental and numerical simulation results. (a) Variations of the initial angular velocity with the step depth. (b) Variations of the initial angular velocity with the step depth.

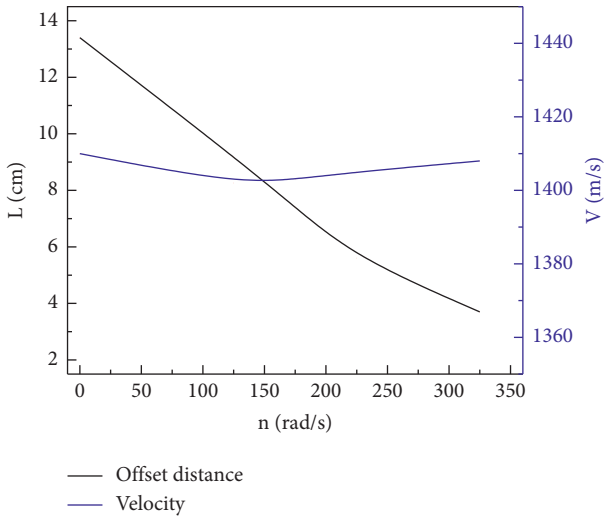

Figure 17: Relationship between the angular velocity and the landing accuracy.

landing point and the target point continually decreased. Thus, when the step angle and step depth were within certain ranges, a greater angular velocity led to a higher landing accuracy. Based on the shock wave generated by the EFP warhead [26, 27] (Figures 16(a) and 16(b)), it was determined that the EFP was flying at a supersonic speed. The EFP was affected by the resistance generated by the shock waves and by air and eddy resistance. The EFP tail fin and lateral tail were in the low-pressure region. Because the EFP tail fin had an oblique angle, even when the angle of attack was 0, the tail fin generated a lifting force that counteracted gravity. This force resulted in a smaller deviation in the gravitational direction and thus a smaller deviation from the target point. Moreover, the lifting force produced a rotational moment around the EFP axis, accelerating the rotation of the EFP. The angular moment of inertia increased with an increase in the angular velocity, leading to a precession phenomenon in the presence of air resistance. Thus, the original flight trajectory could be maintained, resulting in a good landing accuracy.

4.3. Parametric Analysis. Because of the good consistency between the experimental and simulation results in terms of the effects of the step depth and step angle on the angular velocity, this section presents further analysis regarding the influence of the wall thickness d, the number of steps a, and the radius of the spherical arc r on the EFP formation characteristics.

4.3.1. Thickness. Figure 18 shows the shape of the step-shaped liner for the wall thicknesses $d = 2.5$, 3.0, 3.5, and 4.0 mm. Figure 19 shows the variations of the angular velocity, axial velocity, tail fin tilt angle, and aspect ratio with the wall thickness.

Figure 19 indicates that as the wall thickness increased, the EFP shape changed from a cylindrical shape (thin and tall) to a spherical cone (wide and flat). Both the EFP closing radius and the width of the tail fin guide groove increased, while the depth decreased.

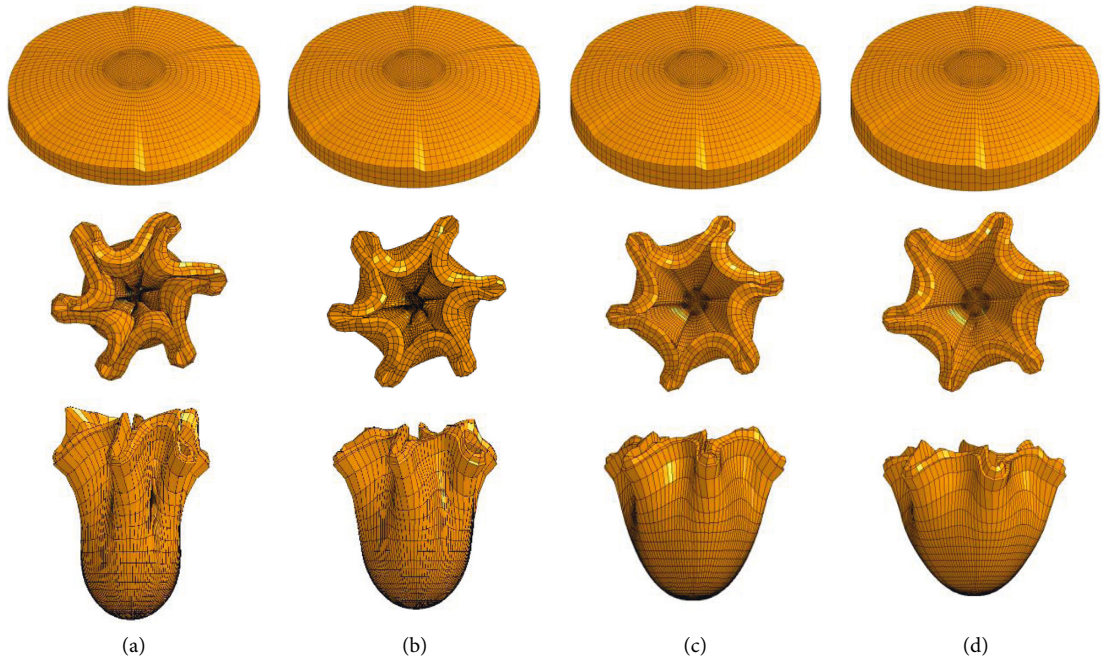

FIGURE 18: EFP formation for different liner wall thicknesses. (a) $d = 2.5$ mm ($t = 240\,\mu$s, $v_a = 1591$ m/s). (b) $d = 3.0$ mm ($t = 240\,\mu$s, $v_a = 1413$ m/s). (c) $d = 3.5$ mm ($t = 240\,\mu$s, $v_a = 1245$ m/s). (d) $d = 4.0$ mm ($t = 240\,\mu$s, $v_a = 1127$ m/s).

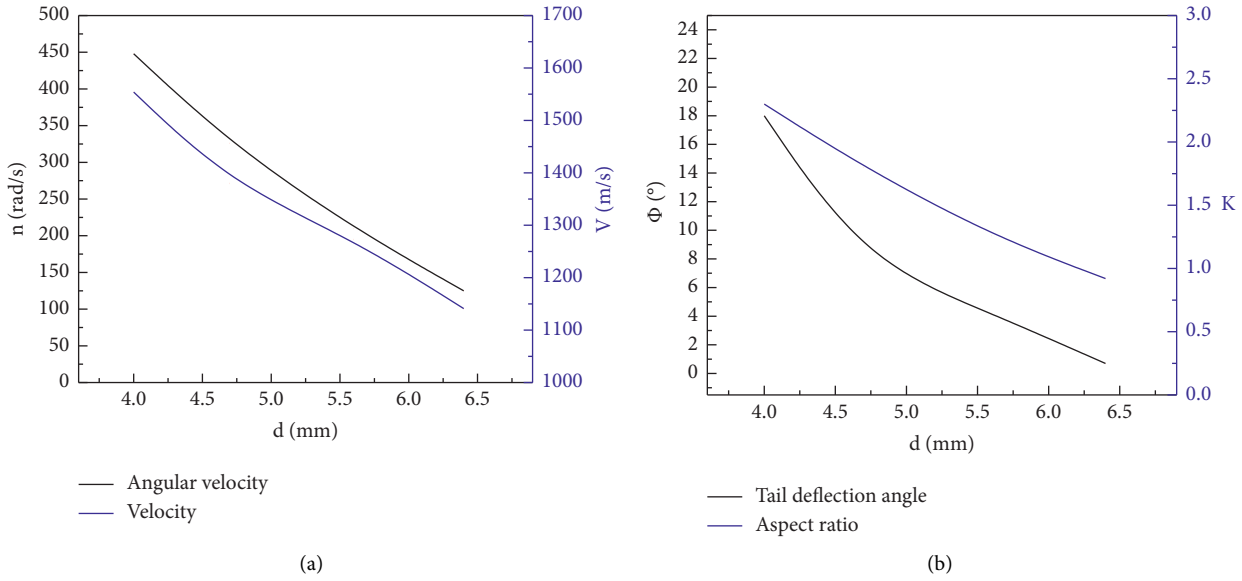

FIGURE 19: Variations of the angular velocity, axial velocity, tail fin tilt angle, and aspect ratio with the liner wall thickness. (a) Variations of the angular and axial velocities with the wall thickness. (b) Variations of the tail fin tilt angle and the aspect ratio with the wall thickness.

Figure 19(a) shows that as the liner wall thickness increased, the EFP formation speed and angular velocity gradually decreased. According to the conservation of momentum between the liner axial velocity and the angular velocity of the radial rotation, the increase in the liner wall thickness led to an increase in its mass. This in turn reduced both the axial velocity and the angular velocity. In addition, Figure 19(b) shows that the tail fin tilt angle and aspect ratio also decreased with an increase in the wall thickness. For the same denotation pressure, an increase in the wall thickness caused reductions in the head velocity gradient and the EFP tail elements. The EFP formed a whole body without much elongation in the axial direction and moved at a constant speed [28]. Thus, the EFP aspect ratio was small. The increase in the wall thickness led to the incomplete formation of the folded EFP tail fins, i.e., a large tail radius and a small tail fin tilt angle.

4.3.2. Number of Steps. A change in the number of steps caused the loading area of the detonation wave on the liner

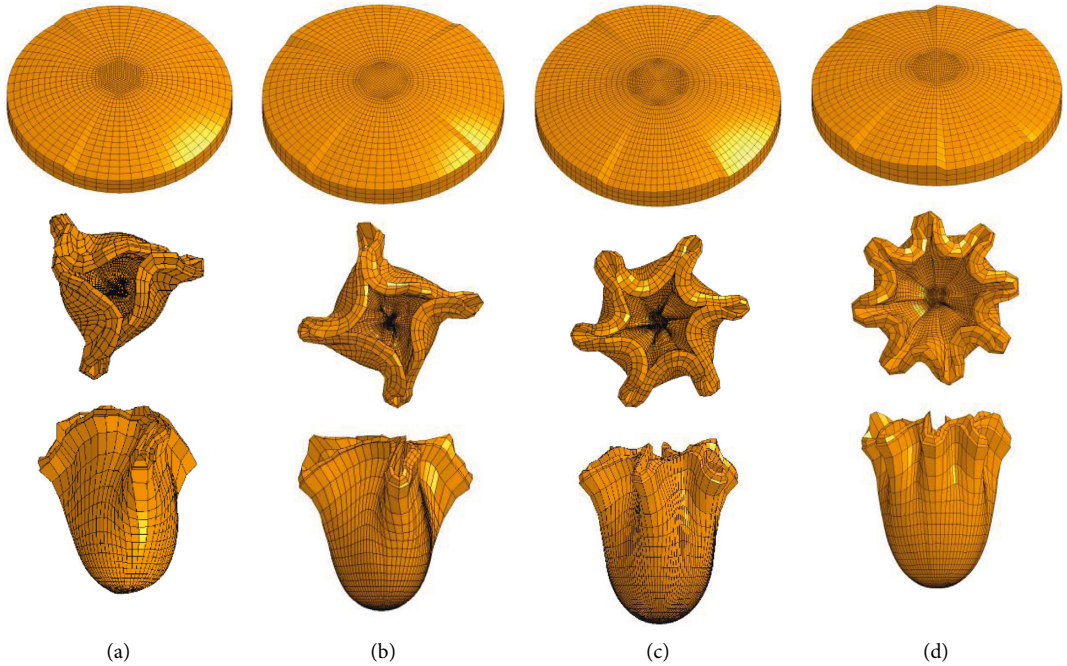

FIGURE 20: Numerical simulation of EFP formation for four different numbers of steps. (a) $a = 3$ ($t = 240\,\mu$s, $v_a = 1403$ m/s). (b) $a = 4$ ($t = 240\,\mu$s, $v_a = 1401$ m/s). (c) $a = 6$ ($t = 240\,\mu$s, $v_a = 1400$ m/s). (d) $a = 8$ ($t = 240\,\mu$s, $v_a = 1399$ m/s).

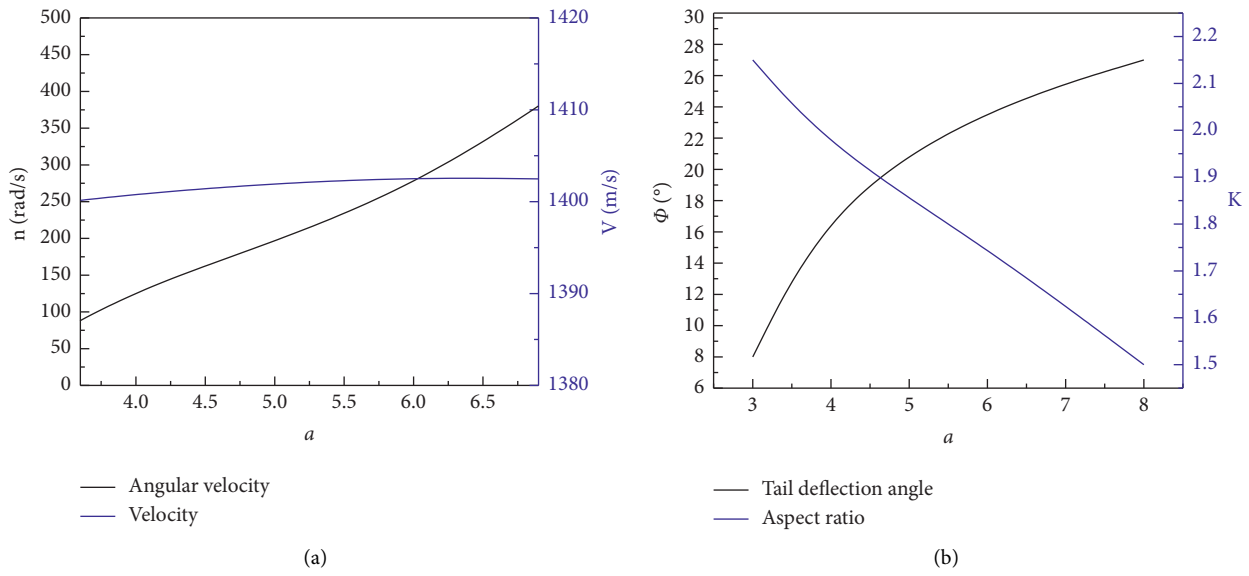

FIGURE 21: Variations of the angular velocity, axial velocity, tail fin tilt angle, and aspect ratio with the number of steps. (a) Variations of the angular and axial velocities with the number of steps. (b) Variations of the tail fin tilt angle and the aspect ratio with the number of steps.

side to change, which in turn affected the EFP formation characteristics. Figure 20 shows the EFP shape when there were 3, 4, 6, and 8 steps. Figure 21 shows the variations of the angular velocity, axial velocity, tail fin tilt angle, and aspect ratio with the number of steps.

Figure 20 indicates that with an increase in the number of steps, the radius of the EFP tail increased, the width and depth of the tail fin guide grooves decreased, and the degree of tail fin convexity in the radial direction decreased.

Figure 21(a) shows that with an increase in the number of steps, the EFP formation speed was nearly unchanged, though the angular velocity gradually increased. According to the conservation of momentum, the axial velocity, mass of the liner, and axial velocity of the EFP were unchanged. However, an increase in the number of steps caused a larger total area of the slope. For the same detonation pressure [29, 30], the tangential rotational torque of the liner increased, and thus, the angular velocity of the EFP also

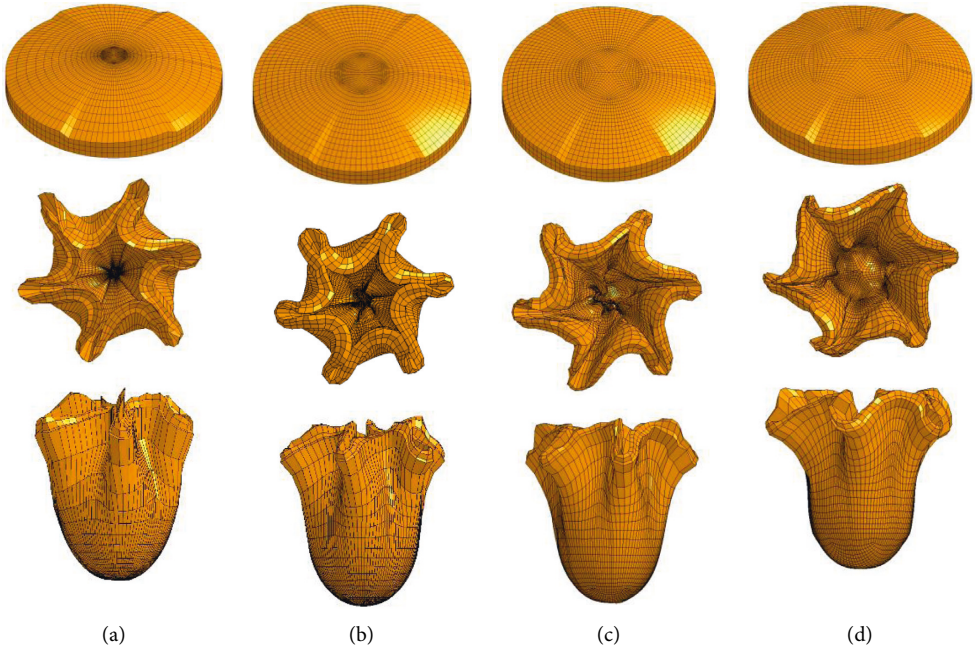

FIGURE 22: Numerical simulation results of EFP formation for four different spherical arc radii. (a) $r = 2.5$ mm ($t = 240\ \mu$s, $v_a = 1410$ m/s). (b) $r = 5$ mm ($t = 240\ \mu$s, $v_a = 1403$ m/s). (c) $r = 7.5$ mm ($t = 240\ \mu$s, $v_a = 1390$ m/s). (d) $r = 10$ mm ($t = 240\ \mu$s, $v_a = 1381$ m/s).

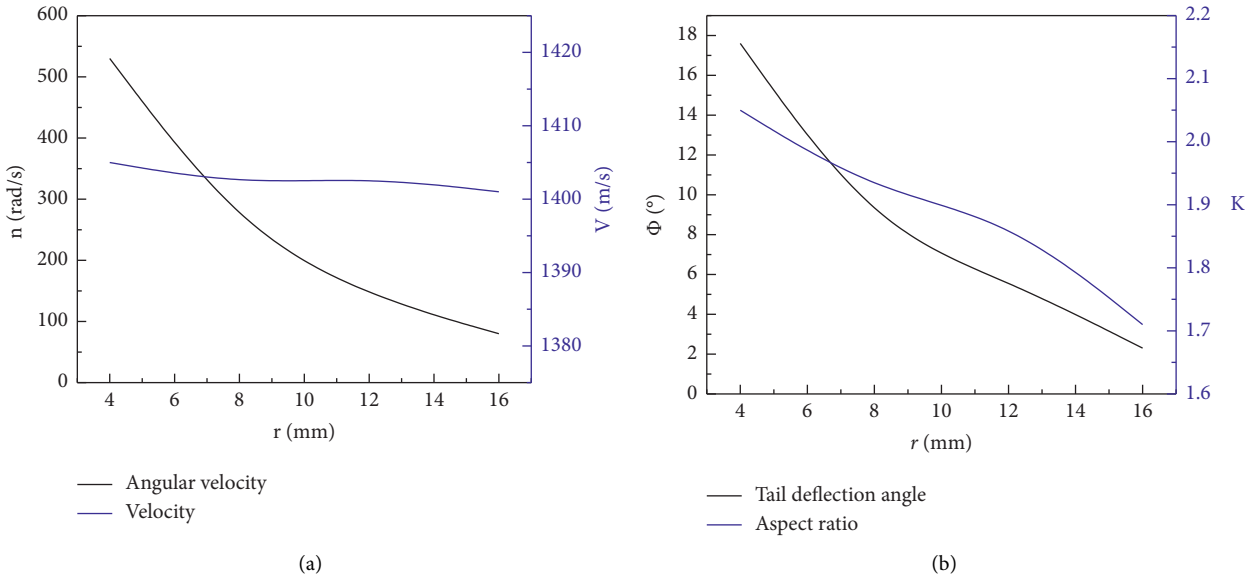

FIGURE 23: Variations of the angular velocity, axial velocity, tail fin tilt angle, and aspect ratio with the spherical arc radius. (a) Variations of the angular and axial velocities with the spherical arc radius (b) Variations of the tail fin tilt angle and the aspect ratio with the spherical arc radius.

increased during the same action time of the detonation pressure. Figure 21(b) indicates that the EFP tail fin tilt angle gradually decreased with an increase in the number of steps. This was because, for the same detonation pressure, the increase in the number of steps led to a decrease in the arc area ratio on the two sides of the steps. When the folded EFP tail fin was formed, the relative displacements of the arc surface elements on the sides of the steps were reduced, and the inclination angles of the convex fins in the radial direction decreased. The EFP aspect ratio gradually increased with the number of steps. This was because the increase in the number of steps led to a circular distribution of the EFP tail fins, thereby reducing the tail fin diameter and increasing the EFP aspect ratio.

4.3.3. Spherical Arc Radius. A change in the spherical arc radius at the top of the liner caused the loading area of the detonation wave on the slope of the steps to change, which in turn affected the EFP formation characteristics. Figure 22

shows the EFP shape for spherical arc radii of 2.5, 5, 7.5, and 10 mm. Figure 23 shows the variations of the angular velocity, axial velocity, tail fin tilt angle, and aspect ratio with the spherical arc radius.

Figure 22 shows that with an increase in the radius of the spherical arc at the top of the liner, the radius at the tail of the EFP increased. The radial length of the tail fin guide groove decreased, the width increased, and the depth decreased. The radial convex size of the folded tail fin also decreased. The formation position of the EFP tail fin was closer to the tail, and the EFP tail diameter gradually increased.

Figure 23(a) shows that with an increase in the radius of the spherical arc at the top of the liner, the EFP velocity remained essentially unchanged, and the angular velocity gradually decreased. The increase in the spherical arc radius at the top of the liner reduced the total area of the slope of the steps. For the same detonation pressure and time, the tangential rotational torque of the liner was reduced, and the EFP angular velocity decreased. Figure 23(b) shows how the EFP tail fin tilt angle gradually decreased with an increase in the radius of the spherical arc. This was because of the reduced slope area on both sides of the steps. The momentum of the denotation wave through the elements on both sides of the steps decreased such that the tail fin inclination angle in the radial direction decreased. In addition, an increase in the spherical arc radius led to a delayed formation of the EFP tail fins, resulting in an EFP tail that was not fully retracted in the radial direction, which in turn led to an increase in the tail diameter and a decrease in the EFP aspect ratio.

5. Conclusions

This study analyzed the explosive forming process of tail fin-type EFPs by theoretical analysis, numerical simulations, and experiments, and the following conclusions were obtained.

(1) A T2 copper step-shaped charge performed better during EFP formation than an H90 brass charge. Compared with a hemispherical liner with an equal wall thickness, the step-shaped liners formed EFPs with a certain initial angular velocity, and there was an improvement in the flight stability and landing accuracy. Moreover, a greater initial angular velocity led to a straighter trajectory, resulting in a higher EFP landing accuracy.

(2) The step depth h, step angle Φ, spherical arc radius r, number of steps a, and wall thickness d were key factors affecting the number of tail fins, tail fin angle, initial angular velocity, flight velocity, and aspect ratio during EFP formation. Meanwhile, the changes in these parameters have a decisive role in determining the flight stability of the EFP. Within a certain range, the initial EFP angular velocity increased with increases in the step depth, step angle, and number of steps and decreased with increases in the spherical arc radius and wall thickness.

(3) The numerical simulation method and the theoretical model of the drug cover molding used in the study had good consistency with the experimental results. The numerical simulation method and the theoretical model of the drug cover molding have application and promotion value in this industry.

Data Availability

Previously reported numerical simulations of data were used to support this study and are available at doi: 10.11809/bqzbgcxb2021.03.008. These prior studies are cited at relevant places within the text as references [20]. In addition, the authors declare that all data in this article are public.

Conflicts of Interest

The authors declare that they have no conflicts of interest.

References

[1] N. William, R. Benard, and V. Eric, "EFP with cantered fins," in *Proceedings of the 19th international symposium on Ballistic*, Interlaken: Switzerland, 2001.

[2] C. Berner and V. Flec, "Pleat and asymmetry effects on the aerodynamics of explosively formed penetrators," in *Proceedings of the 18th International Symposium on Ballistics*, pp. 11–19, TX institute for Advanced Technology-The University of Texas at Austin Southwest Research Institute, San Antonio, 1999.

[3] O. Donneaud, "EFP shape optimization in accordance with information aerodynamics and terminal ballistics aspects," in *Proceedings of the 17th International Symposium on Ballistics*, The South African Ballistics Organization, Midrand, South Africa, March 1998.

[4] Z. X. Yang, Z. G. Chen, B. L. Yang et al., "Numerical simulation on forming and penetration performance of stepped double-layer EFP," *Journal of Ordnance Equipment Engineering*, vol. 43, no. 3, pp. 79–86, 2022.

[5] J. Wu, J. Liu, and Y. Du, "Experimental and numerical study on the flight and penetration properties of explosively-formed projectile," *International Journal of Impact Engineering*, vol. 34, no. 7, pp. 1147–1162, 2007.

[6] G. Hussain, A. Hameed, P. Barton, A. Q. Malik, M. B. Khan, and A. Hussain, "Liner material's output characteristics of explosively formed projectiles (EFPs)," *Key Engineering Materials*, vol. 510-511, pp. 148–155, 2012.

[7] G. Hussain, A. Hameed, J. G. Hetherington, A. Q. Malik, and K. Sanaullah, "Analytical performance study of explosively formed projectiles," *Journal of Applied Mechanics and Technical Physics*, vol. 54, no. 1, pp. 10–20, 2013.

[8] W. Li, X. Wang, W. Li, and K. Chen, "Research on the skirt tail explosively formed projectile stable shaping technology," *Journal of Applied Mechanics and Technical Physics*, vol. 57, no. 5, pp. 894–899, 2016.

[9] W. B. Li and X. M. Wang, "The effect of annular multi-point ini-tiation on the formation and penetration of an explosivelyformed penetrator," *International Journal of Impact Engineering*, vol. 37, pp. 414–424, 2010.

[10] Cardosod and F. Teixeira-Dias, "Modelling the formation of explosively formed projectiles (EFP)," *International Journal of Impact Engineering*, vol. 93, no. 7, pp. 116–127, 2016.

[11] R. Castedo, A. P. P Santos, and J. I. Yenes, "Finite elements simulation of improvised EFP," *Engineering Computations*, vol. 35, no. 8, pp. 2844–2859, 2018.

[12] W. B. Li, X. L. Dong, X. J. Shen, P. Song, and W. X. Xu, "Simulation study on EFP with stable tail fins formed by polygonal shaped charge liner," in *Proceedings of the 31st International Symposium on Ballistics*, Hyderabad, India, November 2019.

[13] M. A. Baburin, V. D. Baskakov, S. V. Eliseev, K. A. Karnaukhov, and V. A. Tarasov, "Influence of geometric features of the peripheral part of the thin-walled spherical segment on the explosive throwing process," *Herald of the Bauman Moscow State Technical University Series Mechanical Engineering*, vol. 2, pp. 76–87, 2020.

[14] L. Ding, J. Jiang, S. Wang, and L. Ji, "Mechanism analysis and prediction of explosive formed projectile's axial fracture," *Modern Physics Letters B*, vol. 36, no. 3, pp. 106–117, 2022.

[15] L. A. Jie, C. B. Xi, and B. Zhd, "A study on the surface overpressure distribution and formation of a double curvature liner under a two-point initiation," *Defence Technology*, vol. 18, no. 1, pp. 10–19, 2022.

[16] Y. Liu, J. Yin, Z. Wang, X. Zhang, and G. Bi, "The EFP formation and penetration capability of double-layer shaped charge with wave shaper," *Materials*, vol. 13, no. 20, p. 4519, 2020.

[17] D. Yang and J. Lin, "Numerical investigation on the formation and penetration behavior of explosively formed projectile (EFP) with variable thickness liner," *Symmetry*, vol. 13, no. 8, pp. 1342–1352, 2021.

[18] B. L. Yang, W. Z. Wang, and J. Tang, "Research on numerical simulation of rotary explosively formed projectile with fins," *Journal of Ordnance Equipment Engineering*, vol. 42, no. 3, pp. 45–50, 2021.

[19] H. M. Li, Z. G. Chen, X. C. Hou, and Numerical simulation of formation mechanism of ladder-shaped rotational EFP, *Journal of Projectiles, Rockets, Missiles and Guidance*, vol. 30, no. 1, pp. 115–118, 2010.

[20] J. Huang and Q. M. Zhang, "Distortion of a liner under sliding detonation," *Journal of Beijing University of Technology*, vol. 29, no. 4, pp. 286–289, 2009.

[21] S. A. Poniaev, R. O. Kurakin, B. I. Reznikov, S. Rozov, B. Zhukov, and M Chernyshov, "Laboratory modelling of an active space experiment using railgun as a launch device," *Acta Astronautica*, vol. 135, no. 4, pp. 63–68, 2017.

[22] J. Q. Liu, W. B. Gu, M. Lu, H. M. Xu, and S. Z. Wu, "Formation of explosively formed penetrator with fins and its flightcharacteristics," *Defence Technology*, vol. 10, pp. 119–123, 2014.

[23] R. Li, W. B. Li, and X. M. Wang, "Influence of three-point detonation control parameters on projectile forming of emtail explosive forming," *Explosion and Shock Waves*, vol. 38, no. 3, pp. 501–508, 2018.

[24] H. Song, C. Li, Y. Xia, J. Wang, and Y. Zhang, "Study of multi-explosively formed penetrators based on the penetration performance and distribution characteristics," *Journal of Applied Mechanics and Technical Physics*, vol. 61, no. 2, pp. 181–188, 2020.

[25] C. X. Zhao, Y. Long, Y. S. Sui, C. Ji, and Z. Xiang, "Influence of initiation methods on formation of integral MEFP warhead parameter," *Journal of PLA University of Science and Technology (Natural Science Edition)*, vol. 13, no. 5, pp. 559–564, 2012.

[26] C. X. Zhao, Y. Long, D. Q. Yu, C. Ji, Y. Y. Zhang, and H. M Xu, "Forming of incised multiple explosively-formed projectiles and their armorpiercing effect against steel target," *Explosion and Shock Waves*, vol. 33, no. 2, pp. 186–193, 2013.

[27] P. Li, B. H. Yuan, and X. Y. Sun, "Experimental research on eccentric initiation MEFP warhead," *Acta Armamentarii*, vol. 38, no. 3, pp. 447–453, 2017.

[28] P. Song, W. B. Li, and X. M. Wang, "Numerical simulation of effects of initiation mode on the performance of circumferential MEFP Warhead," *Journal of Ballistics*, vol. 31, no. 1, pp. 92–96, 2019.

[29] Z. G. Liang and J. W. Jiang, "A numerical analysis on the forming law of circumferential MEFP," *Journal of Projectiles, Rockets, Missiles and Guidance*, vol. 35, no. 2, pp. 57–64, 2015.

[30] Z. G. Liang, B. X. Chen, Y. X. Nan, Jw Jiang, and L Ding, "Research on the computing method for the forming velocity of circumferential multiple explosive formed projectiles," *The Journal of Defense Modeling and Simulation: Applications, Methodology, Technology*, vol. 17, no. 2, pp. 125–136, 2019.